Nano-Micro Letters

ISSN 2311-6706
e-ISSN 2150-5551
CN 31-2103/TB

ARTICLE

https://doi.org/10.1007/s40820-021-00636-0

Cite as
Nano-Micro Lett.
(2021) 13:101

Received: 18 December 2020
Accepted: 5 March 2021
Published online: 1 April 2021

cPCN-Regulated SnO_2 Composites Enables Perovskite Solar Cell with Efficiency Beyond 23%

Zicheng Li[1,2,3], Yifeng Gao[1,3], Zhihao Zhang[1,2,3], Qiu Xiong[1,3], Longhui Deng[1,3], Xiaochun Li[2], Qin Zhou[1,3], Yuanxing Fang[2], Peng Gao[1,3] ✉

HIGHLIGHTS

- The (SnO_2-cPCN) ETL shows superior electron mobility of 3.3×10^{-3} cm^2 V^{-1} s^{-1}, which is about three times higher than that of pristine SnO_2.
- The less wettable SnO_2-cPCN leads to perovskite layers with reduced grain boundaries and enhanced qualities due to suppressed heterogeneous nucleation of perovskite.
- The PSCs based on SnO_2-cPCN showed negligible *J*–*V* hysteresis and two champion PCE of 23.17% and 20.3% on devices with 0.1 and 1 cm^2 active area, respectively.

ABSTRACT Efficient electron transport layers (ETLs) not only play a crucial role in promoting carrier separation and electron extraction in perovskite solar cells (PSCs) but also significantly affect the process of nucleation and growth of the perovskite layer. Herein, crystalline polymeric carbon nitrides (cPCN) are introduced to regulate the electronic properties of SnO_2 nanocrystals, resulting in cPCN-composited SnO_2 (SnO_2-cPCN) ETLs with enhanced charge transport and perovskite layers with decreased grain boundaries. Firstly, SnO_2-cPCN ETLs show three times higher electron mobility than pristine SnO_2 while offering better energy level alignment with the perovskite layer. The SnO_2-cPCN ETLs with decreased wettability endow the perovskite films with higher crystallinity by retarding the crystallization rate. In the end, the power conversion efficiency (PCE) of planar PSCs can be boosted to 23.17% with negligible hysteresis and a steady-state efficiency output of 21.98%, which is one of the highest PCEs for PSCs with modified SnO_2 ETLs. SnO_2-cPCN based devices also showed higher stability than pristine SnO_2, maintaining 88% of the initial PCE after 2000 h of storage in the ambient environment (with controlled RH of 30% ± 5%) without encapsulation.

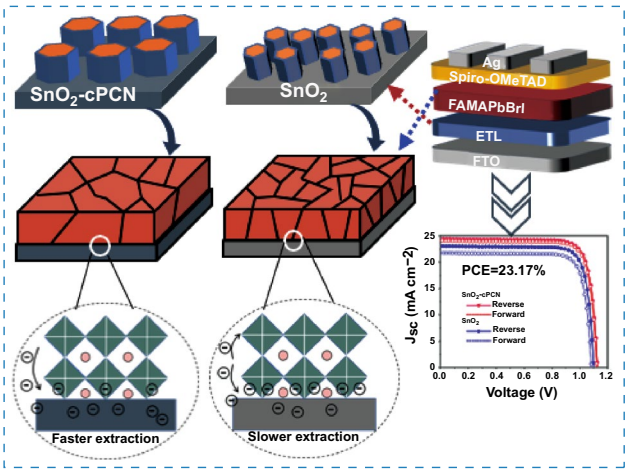

KEYWORDS Electron transport layer; Perovskite solar cell; Carbon nitride; SnO_2

✉ Peng Gao, peng.gao@fjirsm.ac.cn
[1] CAS Key Laboratory of Design and Assembly of Functional Nanostructures, and Fujian Provincial Key Laboratory of Nanomaterials, Fujian Institute of Research on the Structure of Matter, Chinese Academy of Sciences, Fuzhou 350002, Fujian, People's Republic of China
[2] College of Chemistry, Fuzhou University, Fuzhou 350116, People's Republic of China
[3] Laboratory for Advanced Functional Materials, Xiamen Institute of Rare Earth Materials, Haixi Institute, Chinese Academy of Sciences, Xiamen 361021, People's Republic of China

1 Introduction

Organic–inorganic hybrid perovskite-based solar cells (PSCs) are considered the paradigm shift of traditional crystalline silicon photovoltaics due to their fascinating optoelectronic properties and easy solution processability [1–3]. Since the first report in 2009 [4, 5], the certified power conversion efficiency (PCE) of PSCs has exceeded 25%, encouraging the research community to explore further the general principles behind the material design, film formation, device structure, and operational mechanism [6–10]. In the early stage of PSC studies, mesoscopic titanium oxide (m-TiO_2) was frequently used as the electron transport layer (ETL), facilitating the certified world record PCEs [11]. However, the high temperatures (> 500 °C) sintering process damaged the solution processability and limited the application of PSCs in flexible and tandem devices [12]. Besides, the m-TiO_2 presents high photocatalytic activity under the illumination of ultraviolet light, undermining the long-term stability of PSCs [13]. In this regard, planar-type PSCs become potential alternatives to mesoporous types and growing high-quality ETL at low temperatures (≤ 150 °C) has been emphasized to obtain high-efficiency planar-type devices. Among all the candidate ETLs, low-temperature-processed SnO_2 has demonstrated advantages such as high optical transmittance, congruous energy levels, robust chemical and UV stability, and balanced electron mobility (10^{-4} cm^2 V^{-1} s^{-1}) [14–16], enabling several scintillating PSCs with record-breaking performances simultaneously [17, 18].

However, charge accumulation may happen at the SnO_2/perovskite interface resulting in severe hysteresis due to much lower electron mobility of SnO_2 ETL than perovskite absorbers (0.5–30 cm^2 V^{-1} s^{-1}) [19–22]. To alleviate the hysteresis effect, dopants or additives such as metal cations and polymers were added to enhance the conductivity of SnO_2 and hence the PCE of devices. Ren et al. investigated the effect of Nb-doping in SnO_2 and decreased hysteresis due to the enhancement of electron mobility from 1.02×10^{-4} to 2.16×10^{-4} cm^2 V^{-1} s^{-1} [23]. Wei et al. prepared a polymer-incorporated SnO_2 colloidal ink to ameliorate the compactness and wetting property of the SnO_2 layer, and suppressed hysteresis emerged due to better coverage of perovskite film on the SnO_2-in-polymer matrix [24]. The results revealed that the underlayer's surface properties have a crucial influence on the morphology and quality of the perovskite films above.

Shreds of evidence have indicated that these grain boundaries might cause charge recombination ascribed to the presence of charge-trapping recombination centers, and tremendous efforts have been devoted to reducing the grain boundaries of perovskite films. Liu and Huang's groups reported, respectively, that the incorporation of ethylene-diamine-tetra-acetic-acid (EDTA) or red-carbon quantum dots (RCQs) into SnO_2 can increase the wettability at ETL/perovskite interface and generate high-quality perovskite films with enlarged grain size and reduced grain boundaries [15, 19]. In contrast, Huang et al. demonstrated that the non-wetting polymeric HTL surface could also lead to perovskite layers with large grains [25]. Given the discussions above, the surface conditions of the underlayer should be well controlled to generate high-quality and ideally defect-free (less) perovskite films. The influence of the wettability of the underlayer on the perovskite films needs to be further explored.

Targeting the conductivity of SnO_2 and its influence on the quality of the perovskite layer, the presented work realized crystalline polymeric carbon nitride (cPCN)-composited SnO_2 (SnO_2-cPCN) ETL with superior electron mobility of 3.3×10^{-3} cm^2 V^{-1} s^{-1}, which is more than three times higher than that of pristine SnO_2. The PSCs based on SnO_2-cPCN exhibited negligible current density–voltage (*J–V*) hysteresis due to the decreased charge accumulation at the perovskite/ETL interface under the increased electron mobility. Besides, the SnO_2-cPCN surface became smoother and less wettable. On this basis, the perovskite absorber layers with reduced grain boundaries and enhanced qualities were realized due to suppressed heterogeneous nucleation of perovskite. Incorporating cPCN into SnO_2 not only enhanced the electron mobility of ETL via effectively filling the electron trap states but also affected the growth of perovskite grains, reducing non-radiative recombination. Finally, planar PSCs based on SnO_2-cPCN presented a champion PCE of 23.17% on devices with a small active area (0.1 cm^2) and a promising PCE of 20.3% on devices with a large active area (1 cm^2).

2 Experimental Section

2.1 Materials and Reagents

SnO_2 colloid precursor (tin(iv) oxide, 15% in H_2O colloidal dispersion) was purchased from Alfa Aesar. The FAI and MABr were synthesized according to the procedures

https://doi.org/10.1007/s40820-021-00636-0

in previously reported methods. Lead iodide (99.99%) and lead bromide (99.99%) were bought from TCI. The spiro-MeOTAD were bought from Derthon; 4-tert-butylpyridine (96%), bis(trifluoromethane)sulfonimide lithium (LiTFSI) salt (99.95%), chlorobenzene (99.8%), 2N, N-dimethylformamide (99.8%), and dimethyl sulfoxide (99.9%) was purchased from Alfa Aesar.

2.2 Preparation of cPCN and PSCs

2.2.1 Preparations of the g-CN, cPCN

The g-CN powder was synthesized by thermal condensation of the urea. Typically, melamine (8 g) was heated to 500 ºC for 4 h at a rate of 12 °C min^{-1} in a muffle furnace in an air atmosphere. The crystalline PCN was synthesized by an ionothermal approach. In detail, 1.2 g of melamine was mixed with KCl (6.6 g) and LiCl (5.4 g) in a glovebox, and the mixture was then heated to 550 ºC under an N_2 atmosphere (2 L min^{-1}) in a muffle furnace.

2.2.2 Preparations of the SnO_2-cPCN Precursor

The synthesized cPCN NCs powder was first dispersed in deionized water, ultrasonicated for 10 h, and then filtered with a 0.45 mm filter to obtain cPCN NCs water solution of different concentrations. Then, the SnO_2 colloid precursor (15 wt.%) was diluted with deionized water to the concentration of 2.5 wt.% and was stirred at room temperature for 2 h. The cPCN NCs and SnO_2 solutions were mixed with a volume ratio of 1:1 ratio and then ultrasonicated for 1 h.

2.2.3 Device Fabrication

Chemically etched FTO glass substrates were cleaned with a detergent solution, deionized water, acetone, and anhydrous ethanol for 15 min, respectively. Next, the substrates were further cleaned with plasma treatment for 15 min. The SnO_2 solution (Alfa) was spin-coated on the FTO substrates at 3000 rpm for 30 s, followed by annealing at 150 °C for 30 min. The SnO_2-cPCN solution also underwent the same procedures. The substrate was then cool down to room temperature on a spin coater. The $(FAPbI_3)_{0.9}(MAPbBr_3)_{0.1}$ perovskite solution (PbI_2, FAI, $PbBr_2$, MACl, MABr, in DMF: DMSO = 9:1 volume ratio) was spin-coated at 1000 rpm for 10 s and 5000 rpm for 30 s onto the FTO/SnO_2 substrate. 200 µL of chlorobenzene was dropped on the spinning substrate at 8 s before the program finish, and the FTO/SnO_2/perovskite sample was heat-treated at 150 °C for 15 min. Then, the hole transporting layer was deposited on top of the perovskite layer at a spin rate of 4000 rpm for 20 s using a spiro-OMeTAD solution. For the spiro-OMeTAD solution, 72.3 mg of spiro-OMeTAD was dissolved in 1 mL of chlorobenzene with additives of 17.5 µL of bis(trifluoromethylsulfonyl)imide lithium salt (Li-TFSI, Sigma-Aldrich) solution (520 mg mL^{-1} in acetonitrile), 28.8 µL of 4-tert-butylpyridine (TBP, Sigma-Aldrich). Finally, 120 nm of the silver counter electrode was thermally evaporated under a high vacuum.

2.3 Characterization

SEM measurements were performed using a SUPRA 55, Zeiss, Germany, operated at an acceleration voltage of 5 kV. The XRD patterns were measured using a SmartLab X-ray powder diffractometer with an angle range of 2θ = 3° to 60°. UV–vis absorption spectra were recorded on a spectrophotometer (Agilent Cary 5000) in the 350–850 nm wavelength range at room temperature. The steady-state PL spectra were obtained using a fluorescence spectrophotometer (FLS980, Edinburgh Instruments). Current density–voltage (*J-V*) characteristics were measured using a source meter (Keithley 2400) under 100 mW cm^{-2} simulated AM 1.5 G irradiation with a solar simulator (Enli Tech, Taiwan) by reverse (1.2 to -0.1 V) scans or forward scan (from −0.1 to 1.2 V) modes at a scan speed of 200 mV s^{-1}. The hysteresis indices ($H_{hysteresis}$) of the devices are calculated based on Eq. 1.

$$H_{hysteresis} = \frac{PCE_{reverse} - PCE_{forward}}{PCE_{reverse}} \times 100\% \quad (1)$$

The active area of devices was defined by a metal shadow mask of 0.1 or 1 cm^2. The dark current–voltage curves were recorded with an electrochemical workstation (Zennium Zahner, Germany). In detail, the measurement works as follows: For the first edge potential of -1.0 V, the second edge potential of 1.5 V was applied. The EQE was characterized by the QE-R systems (Enli Tech.), and the measurement scope was 300–900 nm. EIS measurements were carried out in the dark at 0.5 V applied voltage using an electrochemical workstation (Zennium Zahner, Germany) with an AC

perturbation of 10 mV ranging from 100 to 1 MHz at room temperature with 60% humidity (Fig. S6). FTIR spectra were recorded on a Nicolet iS 50 Spectrometer. The roughness of the films was recorded using atomic force microscopy (AFM, Multimode-8J, America). The water contact angle was measured at a Data physics OCA-20 drop shape analyzer.

To gain insights into the charge transport, we measured electron mobility using different ETLs in the same device structure. Specifically, the electron-only device was designed and fabricated using FTO/ETL/PCBM/Ag structure, as shown in the inset in Fig. 2b (later). In this analysis, we assumed that the current is only related to electrons. When the effects of diffusion and the electric field are neglected, the current density can be determined by the SCLC [26]. The different ETLs were spin-coated on FTO. Then, 120-nm-thick Ag was deposited on FTO/ETL/PCBM samples. The dark J–V curves of the devices were performed on a Keithley 2400 source at ambient conditions. The electron mobility (μ_e) is extracted by fitting the *J–V* curves using the Mott–Gurney law (Eq. 2):

$$\mu_e = \frac{8JL^3}{9\varepsilon\varepsilon_0(V_{app} - V_r - V_{bi})^2}, \quad (2)$$

where J is the current density, L the thickness of different ETLs, ε_0 the vacuum permittivity, ε_r the dielectric permittivity of various ETLs, V_{app} the applied voltage, V_r the voltage loss due to radiative recombination, and V_{bi} the built-in voltage owing to the different work function between the anode and cathode.

3 Results and Discussion

3.1 Crystalline Polymeric Carbon Nitride Characterization

Carbon derivatives, such as carbon nanotubes, fullerene, and graphene (oxide), have been widely used as additives or interlayers in PSCs [27, 28]. Particularly, traditional graphitic carbon nitride (g-CN) was reported to facilitate high-efficiency PSCs. For example, Jiang et al. added g-CN in precursor solutions to improve the quality and conductivity of perovskite films [29]. Similarly, Li et al. developed a series of functionalized g-CN (SO_3–, OH–, NH_3–, or NO_3–C_3N_4) to modify the perovskite precursor solution and achieved the best PCE of 20.08% with NO_3-C_3N_4 [30]. Recently, Chen et al. used hybrid quantum dots of SnO_2/g-CN was used as the ETL in PSCs and demonstrated that the g-CN could reform the electronic density distribution around the neighboring SnO_2 crystal unit to effectively eliminate the oxygen-vacancy type trap centers and promote the electron transport [31]. Compared with the widely used g-CN, the cPCN is the highly crystalline counterpart with fully conjugated π-electron systems and higher conductivity [32, 33], which may further enhance the functionality of SnO_2 based ETLs. It is worth noting that traditional poly-heptazines are often (and misleadingly) classed as 'graphitic carbon nitride,' 'graphitic CN' or 'g-C_3N_4′ in literature, including our own reports [33]. To that end, we have proposed to correct the term of 'gCN' to 'PCN' in one of our review papers [32].

The preparation protocol of the g-CN and cPCN semiconductor is described in the experimental section. In this study, preheated melamine was used as a precursor in the presence of KCl/LiCl to synthesize cPCN with tri-s-triazine subunits. The high crystallinity nature of cPCN was verified by X-ray diffraction (XRD), as illustrated in Fig. 1a. The cPCN exhibited a narrower and shifted diffraction peak at 28.3° with a full width at half-maximum (FWHM) compared to traditional g-CN (27.4°), indicating the well-developed and condensed crystal structure with enhanced interaction between layers [33]. The peak at 13.0° corresponding to the inter-plane distance of 0.618 nm for g-CN is shifted to 8.0° with a repeat unit of 1.099 nm due to an unfolded in-plane network associated with sufficient condensation of the conjugated framework (Fig. S1) [33]. The FTIR spectra in Fig. 1b further exhibit the structure information of cPCN and g-CN. The broad peaks between 3500 and 3000 cm^{-1} stem from the terminal amino groups, while the peak at 2150 cm^{-1} originates from terminal cyano groups (C≡N) owing to the loss of ammonia on the surface of traditional g-CN [34]. The set of peaks between 1700 and 900 cm^{-1} are characteristic signals from tri-s-triazine derivatives [35].

The as-prepared cPCN sample exhibits porous structures under scanning electron microscopy (SEM) (Fig. 1c). The transmission electron microscopy (TEM) image presents stacked layers of nanosheets (Fig. 1d). The high-resolution TEM images of cPCN are illustrated in Fig. 1e, f, revealing a clear hexagonal lattice structure with two lattice fringes. The lattice fringe of 0.33 nm may be assigned to the interlayer distance, while the 0.98 nm lattice fringe is likely originated from the in-plane periodicity. Furthermore, more

 https://doi.org/10.1007/s40820-021-00636-0

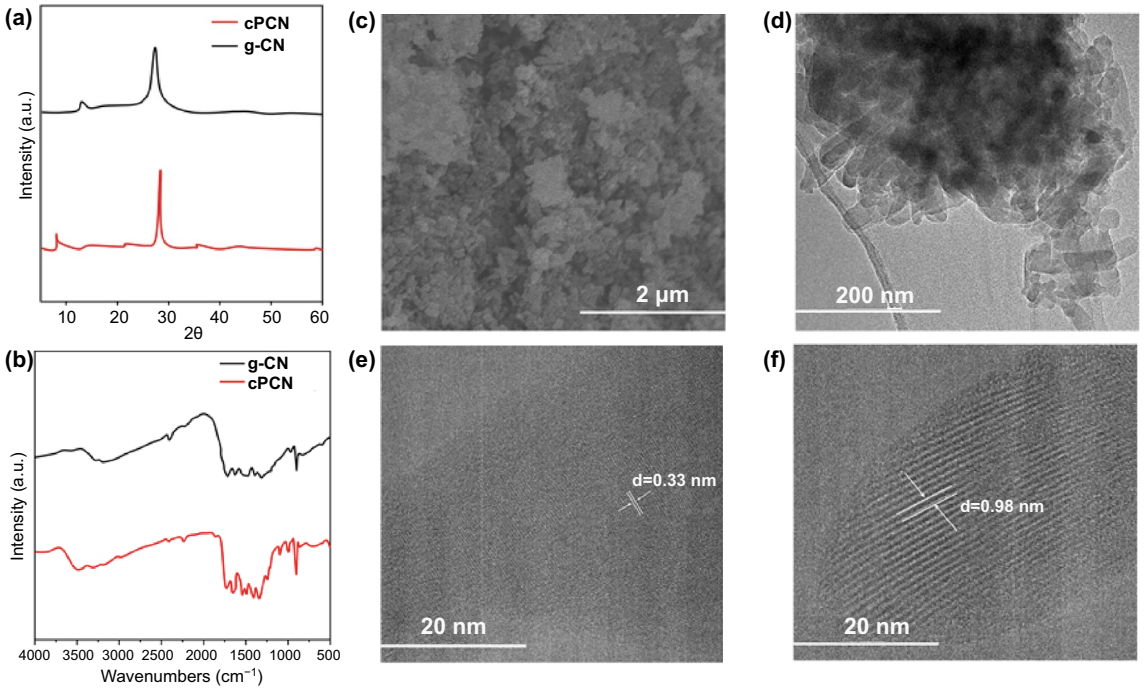

Fig. 1 **a**, **b** XRD patterns and FTIR spectra of cPCN and g-CN. **c** SEM images and **d** TEM images of cPCN. **e, f** HRTEM images for cPCN

information and discussions about the difference between PCN and cPCN, including morphology, structure, optical properties, electrical property, and stability, can be found in one of our works [33].

3.2 Fabrication and Characterization of SnO_2-cPCN Film

We plotted XRD patterns of SnO_2 and SnO_2-cPCN based films to investigate the structural properties and phase composition (Fig. S2). These peaks match well with characteristic diffractions of SnO_2 (JCPDS No. 01-077-0452). Except the signals from the underlying FTO, no obvious peak relating to cPCN, SnO_2, or any other impurity is detected. It is important to note that due to the very thin nature of the deposited layers (ca. 30 nm), minority phases may be challenging to be identified.

Based on the previous studies, the novel cPCN with higher crystallinity and conductivity may have the potential to improve the performance of SnO_2 ETL. Specifically, X-ray photoelectron spectra (XPS) of SnO_2 and SnO_2-cPCN films deposited on quartz substrates are conducted (Figs. 2a and S3) to explore the interactions between cPCN and SnO_2. We calibrated the binding energy scale for all XPS measurements to the carbon 1 s line at 284.8 eV. After the cPCN incorporation, the binding energies of Sn $3d_{3/2}$ and Sn $3d_{5/2}$ at 486.34 and 494.77 eV shift slightly to higher values at 486.52 and 494.87 eV, respectively. The blue shift (toward higher binding energy) of Sn 3d signals indicates the electron transfer and may promote electron mobility [36–39]. Besides, the SnO_2-cPCN film presents two additional peaks at 400.08 and 404.16 eV originating from the N1s of cPCN (Fig. S3a, b). Consequently, the cPCN is successfully composited and chemically bonded with SnO_2.

The speculated enhancement in electron mobility is further confirmed by measuring the *J*–*V* characteristics of electron-only devices with a structure of FTO/ETL/PCBM/Ag based on SnO_2-cPCN and pristine SnO_2. Unless stated otherwise, all the characterizations are based on SnO_2-cPCN films fabricated by adding 0.6 mg mL^{-1} cPCN solution to the colloidal solution of SnO_2. The optimization process toward the highest PSC performance was recorded in the device fabrication section. As illustrated in Fig. 2b, the electron mobility of these two ETLs can be calculated using the space charge-limited current (SCLC)

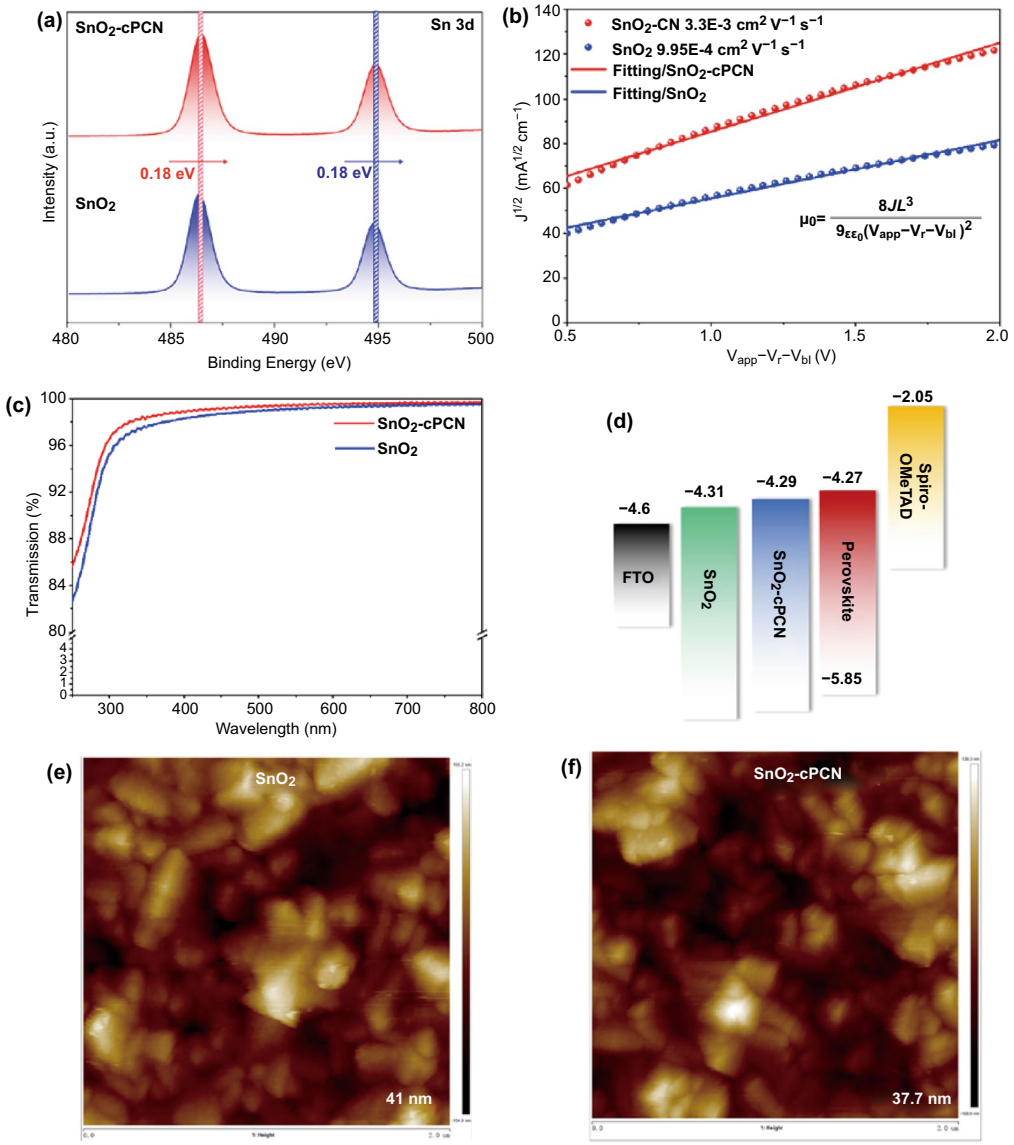

Fig. 2 Characterization of SnO_2 and SnO_2-cPCN ETLs. **a** XPS spectra of films deposited on quartz substrates. **b** Electron mobility calculation using the SCLC model with the device structure of FTO/ETL/PCBM/Ag. **c** Optical transmission spectra on quartz substrates. **d** Possible band alignment of the ETLs and perovskite layer according to the UPS measurements. **e**, **f** AFM topographical images of SnO_2, and SnO_2-cPCN films

model fitted by the Mott–Gurney law [40, 41]. The electron mobility of SnO_2-cPCN was 3.3×10^{-3} cm^2 V^{-1} s^{-1}, which was one magnitude larger than those of pristine SnO_2 (9.95×10^{-4} cm^2 V^{-1} s^{-1}). This is consistent with the conclusion of the XPS test. Considering that the carbon and nitrogen atoms of cPCN are sp^2-hybridized to form fully π-conjugated electronic structures, we speculate that the excess electron traps in SnO_2 could be consumed under the electron-rich conditions [27], which consequently increased the mobility and decreased the work function [36]. This, in turn, led to different way of band-bending and resulted in a decrease of the energy barrier at the SnO_2/perovskite interface [36, 42], which can significantly affect charge extraction, collection, and recombination in PSC. The higher electron mobility can effectively facilitate electron transfer in the PSCs, reduce charge accumulation at the ETL/perovskite interface, improve efficiency, and suppress hysteresis in the PSCs [43]. Additionally, the optical transmission spectra of SnO_2 and SnO_2-cPCN films coated on quartz substrates are presented in Fig. 2c. Both

 https://doi.org/10.1007/s40820-021-00636-0

samples exhibit high average transmittance in the visible region, demonstrating excellent optical quality to pledge that most light can pass through and be absorbed by the perovskite layer.

Ultraviolet photoelectron spectroscopy (UPS) measurements are performed to estimate band position shifts after hybridizing cPCN in SnO_2 (Fig. S4a). According to the formula of work function (WF) = 21.22 eV − E_{cutoff} (cutoff binding energy), the WF of SnO_2-cPCN is calculated to be − 4.32 eV. Then, the E_{VBM} of SnO_2-cPCN can be calculated to be − 8.08 eV by E_{VBM} = WF—$E_{F, edge}$ (Fermi edge). It was reported that the WF, conduction band (E_{CBM}), and bandgap (E_g) of the SnO_2 nanoparticles were − 4.36, − 4.31, and 3.79 eV, respectively [44]. Therefore, the E_{CBM} values of SnO_2-cPCN can be calculated to be − 4.29 eV considering that the bandgap (~ 3.79 eV) of SnO_2 films is not changed with or without cPCN. According to the theory study in literature [31], we reasonably speculate that the fully conjugated structure of cPCN changes the surface electron density of SnO_2, resulting in such shift in the energy band of SnO_2. Subsequently, the E_{CBM} values of perovskite are deduced using the same method to be − 4.27 eV with an E_g of 1.58 eV (Fig. S4b) [6]. The energy band diagram for a typical n-i-p PSC device (Fig. 2d) indicates that the SnO_2-cPCN ETL is more favorable as an effective electron extraction channel conducive to reducing V_{OC} loss.

To ascertain the change in film morphology of ETL after hybridization, we show atomic force microscopy (AFM) and scanning electron microscope (SEM) images of the SnO_2 and SnO_2-cPCN films deposited on the FTO substrates in Figs. 2e, f and S7, respectively. The SnO_2-cPCN film turns out to have a similar root-mean-square (RMS) roughness (37.7 nm) as that of the control film (41 nm). In Fig. S5, the water contact angle/perovskite solution of the SnO_2-cPCN film is measured as 41°/47°, which is much larger than that of the pristine SnO_2 (33.5°/38°). Furthermore, the contact angle of both films also is obtained after UV-ozone treatment and show the same trend (Fig. S6). According to the previous report [25], the non-wetting under-layer may lead to the formation of perovskite films with high-aspect-ratio crystalline grains since the lessened dragging force can result in high grain-boundary mobility [45]. Besides, Deng et al. further proposed that the attraction between the solute ions and solvent molecules on the hydrophilic surface was comparably stronger than the hydrophobic surface [46]. The strong attraction of the surface to the pre-existing clusters will fix more clusters on the substrate surface and block the re-dissolution of ions from pre-existing cluster surfaces. So, the existing cluster becomes more stable and easier to grow into crystal nuclei. In addition, the reaction heat released during cluster growth can be dissipated more rapidly through the surfaces due to a relatively higher interaction intensity, which is beneficial to the formation of the nucleus. Meanwhile, the precursor ions and solvent that are close to the surface will be attracted and then captured by the hydrophilic surface, which will slow down the diffusion of ions, leading to a slower crystal growth rate and smaller grain size [46–48]. Conversely, the non-wetting (hydrophobic) substrates can provide a higher free-energy barrier for nucleation, faster crystal growth rate, larger grain size, and less grain boundary [49, 50].

3.3 Fabrication and Characterization of Perovskite Solar Cells

3.3.1 Perovskite Film Characterization

Generally, the quality of perovskite films can be defined by some conspicuous features, such as grain size, crystallinity, and surface coverage, which collectively affect the performance of perovskite solar cells. Specifically, the topographic SEM images of perovskite films (prepared with the same composition and process) deposited on SnO_2 and SnO_2-cPCN are exhibited in Fig. 3a, b to investigate the influence of SnO_2-cPCN hybridization on the morphology and crystallization of the perovskite films atop. Both films present dense and uniform morphology, with randomly interconnected grains. The statistical size distributions of perovskite grain clusters on different ETLs are plotted in Fig. S8. The perovskites deposited on SnO_2 possessed an average grain size of about 1.08 μm. As the cPCN is incorporated into the SnO_2, the appearance of pinholes decreased, and the average grain size significantly increased to 1.66 μm. These phenomena validated that more non-wetting surface after introducing cPCN did enlarge the grain size and decrease the grain boundaries of perovskite, in accord with the contact angle test.

To further study the effect of the cPCN incorporation on the solid structure of perovskite films, we collected XRD patterns of the perovskite films on two kinds of ETLs. It can be observed in Fig. 3c that both samples present a cubic

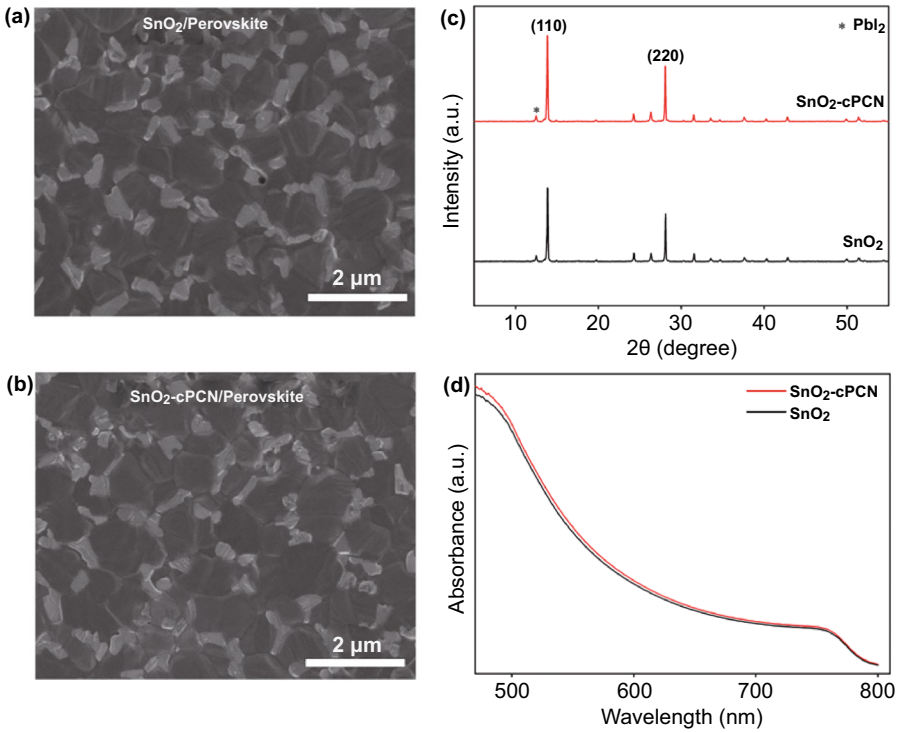

Fig. 3 Top view SEM images of perovskite films coated on **a** SnO_2 and **b** SnO_2-cPCN substrates. **c** XRD patterns and **d** UV–Vis spectra of the perovskite films on SnO_2 and SnO_2-cPCN

perovskite phase structure, in which the prominent peaks around 13.98° and 28.22° correspond to the (110) and (220) planes. The diffraction peak at 12.6° in all films belongs to the PbI_2 phase [45]. When cPCN was added, the intensity of (110) and (220) diffractions are enhanced, and the calculated full width at half maximum (FWHM) of (110) diffraction becomes smaller (0.112°) compared with the pristine sample (0.129°), suggesting a better-grown film with improved crystallinity. Subsequently, the UV–visible absorption spectra of the perovskite film grown on SnO_2-cPCN further demonstrates slightly higher absorbance than that of the pristine film (Fig. 3d), contributing to enhancing photocurrents in the PSCs (vide infra).

3.3.2 Photovoltaic Performance

The photovoltaic performance of the novel SnO_2-cPCN ETL based PSCs was examined by fabricating a series of $(FAPbI_3)_{0.9}(MAPbBr_3)_{0.1}$-based planar-type PSCs with a structure of FTO/ETL/perovskite/Spiro-OMeTAD/Ag, as exhibited in the inset of Fig. 4a. The optimization results of cPCN concentrations in SnO_2 colloidal are provided in Fig. S9 and Table S1. Besides, the current density versus voltage (*J–V*) characteristics for the champion PSCs based on the SnO_2 and SnO_2-cPCN ETLs under AM 1.5G illumination (100 mW cm^{-2}) are illustrated in Fig. 4a. The main cell parameters of V_{OC}, J_{SC}, *FF*, and *PCE* are summarized in Table 1. The device based on the pristine SnO_2 substrate presentes a PCE of 21.3% with J_{SC} of 23.4 mA cm^{-2}, V_{OC} of 1.11 V, and *FF* of 82%. After optimization, the best device ($0.1cm^2$) is obtained with a *PCE* of 23.17%, a V_{OC} as high as 1.126 V, a J_{SC} of 24.9 mA cm^{-2}, and *FF* of 82.5%. It is one of the best performances in PSCs with modified SnO_2 [15, 51, 52]. The superior performance of PSCs with cPCN-treated SnO_2 is in line with the improved film quality and higher absorptions. In Fig. 4b, the incident photon-to-current efficiencies (IPCE) of the optimal solar cells based on SnO_2-cPCN show significant enhancement over 400–770 nm wavelength than that based on unmodified SnO_2, which can be attributed to the enhanced UV–visible absorption spectra of the perovskite film grown on SnO_2-cPCN with improved crystallinity (Fig. 3c). The integrated J_{SC} of 23.94 and 22.45 mA cm^{-2} for PSCs with SnO_2-cPCN and SnO_2 can be

 https://doi.org/10.1007/s40820-021-00636-0

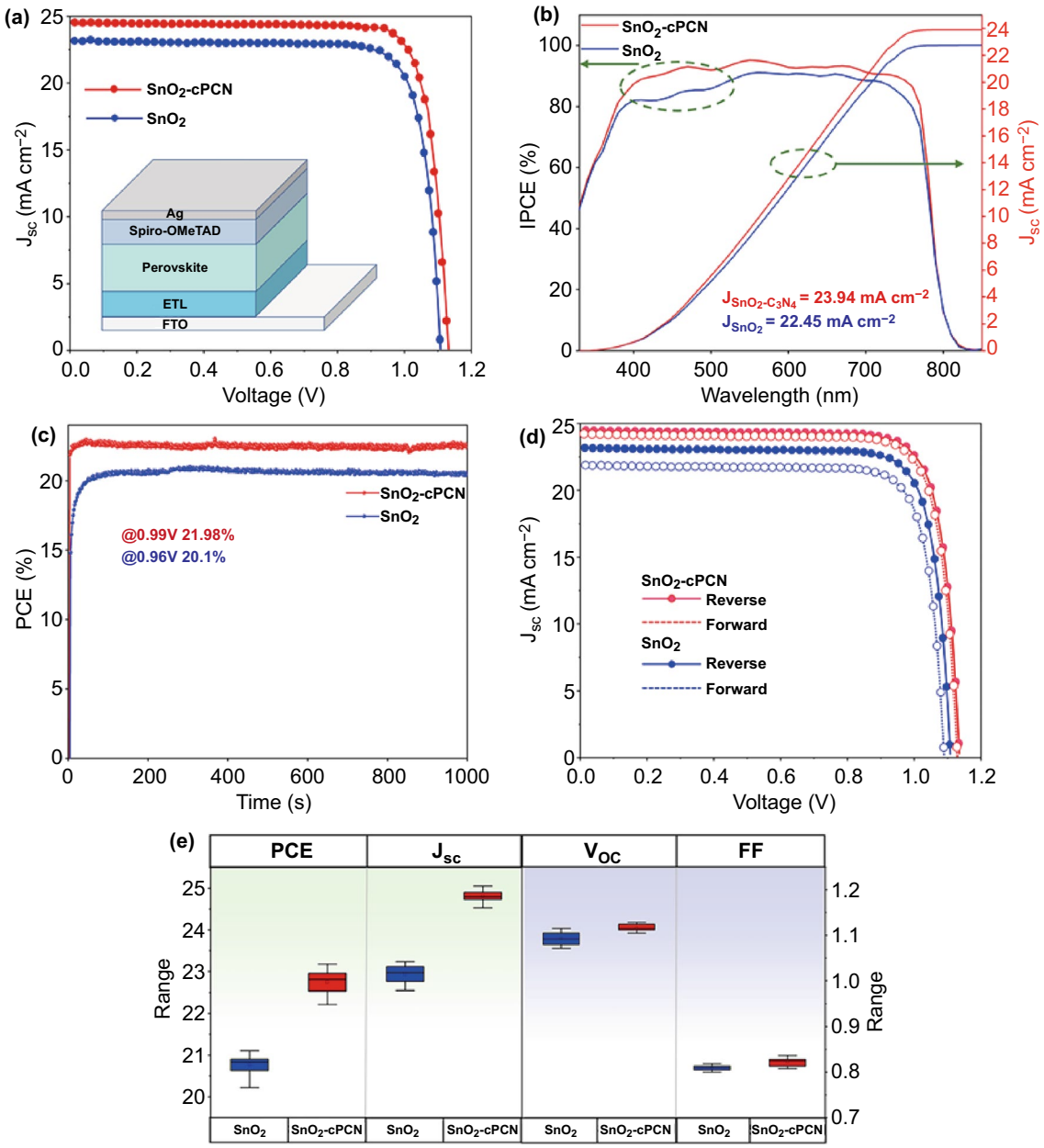

Fig. 4 **a** *J–V* characteristics for champion PSCs based on the SnO_2 and SnO_2-cPCN ETLs under the illumination of 1 sun (AM 1.5 G). **b** Corresponding EQE curves and integrated current density of the two champion PSCs. **c** The stabilized power output of the fabricated PSCs on the SnO_2-cPCN and SnO_2 ETL at the maximum power point (MPP) at 0.99 and 0.96 V. **d** *J–V* curves of both champion devices for both forward and reverse scans. **e** Distribution of photovoltaic parameters of the two kinds of solar cells (20 devices for each case)

calculated and in acceptable agreement with the *J–V* results. The increase of J_{SC} mainly originates from the improved band alignment, better carrier transport from perovskite to ETLs, and enhanced light absorbance. The stabilized power output (SPO) of PSCs was performed to determine the power output stability of the devices at the maximum power point (MPP) under AM 1.5G illumination (Fig. 4c). The output PCE of the sample with SnO_2-cPCN as the ETL is traced for 1000 s at MPP (0.99 V), and a stabilized *PCE* of 21.98% can be recorded, matching the PCE value extracted from the *J–V* curve. For the control device, a stabilized PCE of 20.1% at the maximum power point (0.96 V) is recorded

Table 1 Device performance of champion PSCs based on SnO_2 and SnO_2-cPCN ETLs

ETLs	Area (cm^2)	Scan direction	V_{OC} (V)	J_{SC} ($mAcm^{-2}$)	*FF* (%)	*PCE* (%)	*HI* (%)
SnO_2	0.1	Reverse	1.11	23.4	82	21.3	6.5
		Forward	1.1	22.4	80.5	19.9	
SnO_2-cPCN	0.1	Reverse	1.126	24.9	82.5	23.17	1.5
		Forward	1.125	24.7	82	22.8	
	1	Reverse	1.13	24	75	20.3	0.4
		Forward	1.12	23.9	75.5	20.2	

over the same period. Notably, the SnO_2-cPCN based device has a much faster response of less than 8 s to reach the SPO point than the pristine device (80 s) ascribed to the reduced trap-assisted recombination and the enhancement of electron mobility caused by the incorporation of cPCN [53].

Ion migration, high trap density, and unbalanced charge transport are currently considered the main reasons for the hysteresis [54, 55]. To investigate the hysteresis effect in our system, we measured *J-V* curves along with both bias scanning directions in Fig. 4d and Table 1. The hysteresis indices ($H_{hysteresis}$) of the devices were calculated based on Eq. 1 [56]. Besides, the device using SnO_2-cPCN ETL shows negligible hysteresis, contrasting to the much larger effect with the SnO_2 ETL. The crucial role of SnO_2-cPCN in resolving the hysteresis issue was also checked with transient photocurrent decay (TPC) and photovoltage decay (TPV) (Fig. S10a, b). It is revealed that the time constant of the photocurrent decay significantly decreases while the decay time of the photovoltage increases when the device was fabricated based on SnO_2-cPCN ETL. Due to the comparable electron mobility of SnO_2-cPCN ETL (3.3×10^{-3} cm^2 V^{-1} s^{-1}) to the hole mobility of the doped spiro-OMeTAD (~ 10^{-3} cm^2 V^{-1} s^{-1}), the electron flux (Fe) is essentially equal to the hole flux (Fh) considering that the interface areas of both ETL/perovskite and perovskite/HTL are the same. Therefore, charge accumulation on either side of the devices based on the SnO_2-cPCN can be alleviated, which, consequently, exhibit negligible hysteresis (Fig. S11) [19, 57]. In addition, we speculate that the K^+ in carbon nitride may also contribute to the reduced hysteresis in the devices [58, 59]. The statistical analysis of all parameters (V_{OC}, J_{SC}, *FF*, and *PCE*) of PSCs based on SnO_2 and SnO_2-cPCN are provided in Fig. 4e (20 cells counted for each case). Fascinatingly, the devices based on SnO_2-cPCN exhibite excellent repeatability with a minimal standard deviation and reliability in contrast to the devices based on unmodified SnO_2.

3.3.3 Charge transfer dynamics

Further insights into the origin of the performance enhancement for the device using SnO_2-cPCN ETL can be obtained from the thermal admittance spectroscopy (TAS) measurement by examining the trap density of states (tDOS) in the devices with and without cPCN (Fig. 5a). TAS is a well-established, effective technique for characterizing both shallow and deep defects and has been broadly adopted to understand defects in the thin film [60, 61]. The defect density (N_T) can be estimated by Eq. 3:

$$N_T(E_\omega) = -\frac{V_{bi}}{qW}\frac{dC}{d\omega}\frac{\omega}{TK_B} \quad (3)$$

where C is the capacitance, ω is the angular frequency, q is the elementary charge, k_B is the Boltzmann's constant, and T is the temperature. V_{bi} and W represent the built-in potential and depletion width, respectively, and can be obtained from the previous report [62]. The applied angular frequency ω defines the energetic demarcation,

$$E_\omega = K_B T \ln\left(\frac{\omega_0}{\omega}\right), \quad (4)$$

where ω_0 denotes the attempt-to-escape frequency and can be output by frequency-dependent capacitance plot [63]. As illustrated in Fig. 5b, the devices with SnO_2-cPCN ETL have dramatically lower trap density than the SnO_2 ETL (above 0.4 eV). This demonstrates that the perovskite grown on SnO_2-cPCN ETL possesses reduced deep-level defects at the grain boundary due to the enhanced grain size, contributing to reducing the recombination of carriers and enhancing the performance of PSCs device dramatically [64, 65]. Furthermore, the electron-only devices with the structure of FTO/ETL/Perovskite/PCBM/Ag were also manufactured for space charge limited current (SCLC) measurement as circumstantial evidence to the decreased trap density of perovskite deposited on SnO_2-cPCN. The dark current–voltage (*I–V*) curves are illustrated in Fig. S12a, b. The trap densities

https://doi.org/10.1007/s40820-021-00636-0

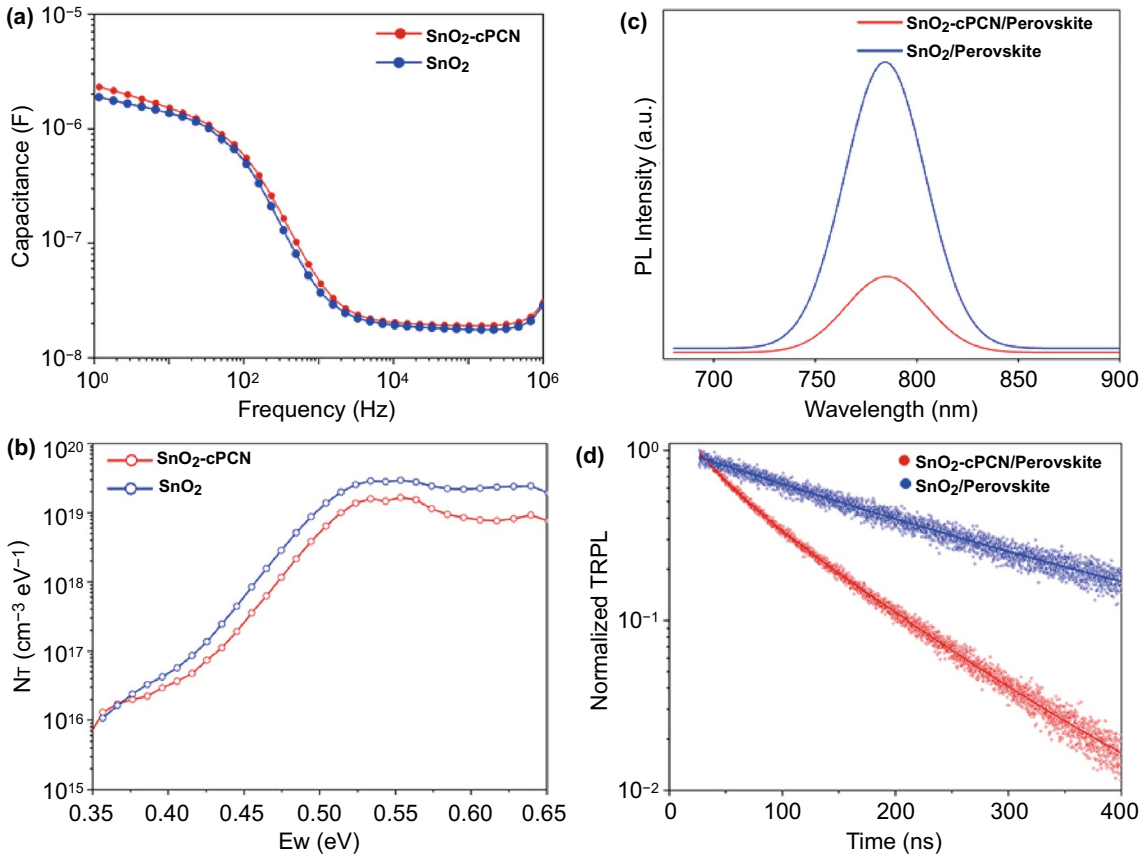

Fig. 5 **a** Frequency-capacitance measured from perovskite devices on the SnO_2-cPCN and SnO_2 ETL. **b** Trap density of states (tDOS) for devices with SnO_2-cPCN and SnO_2 ETL. **c** Steady-state PL and **d** TRPL spectra of perovskite films deposited on different substrates

of the perovskite film coated on SnO_2 and SnO_2-cPCN substrates are 1.75×10^{16} and 8.39×10^{15} cm^{-3}, respectively. The reduced trap density is consistent with TAS measurement.

The charge carrier recombination dynamics of the perovskites deposited on different ETLs were investigated by steady-state photoluminescence (PL) and time-resolved photoluminescence (TRPL) decay measurements. The characteristic PL spectra of all the perovskite films are located at around 784 nm (Fig. 5c). Compared with the pristine sample, the PL intensity of SnO_2-cPCN based perovskite films is much weaker, demonstrating enhanced charge extraction with reduced recombination, leading to increased photocurrents in the PSCs [53]. For the TRPL spectra in Fig. 5d, all TRPL curves are fitted by a biexponential function as follows:

$$y = A_1 \times e^{-t/\tau_1} + A_2 \times e^{-t/\tau_2} + A_0, \quad (5)$$

where A_1 and A_2 denote the relative amplitude fractions for τ_1 and τ_2, respectively. Generally, the fast decay lifetime (τ_1) results from the trap-assisted recombination at the interface, and the slow decay lifetime (τ_2) is related to the biomolecular recombination of photogenerated free carriers due to traps in bulk [66, 67]. The fast decay component (τ_1) for perovskite film deposited on the SnO_2 layer is 176 ns. After cPCN is incorporated into the SnO_2 layer, τ_1 is shortened to 30 ns, confirming the much faster charge extraction and transport through the SnO_2-cPCN compared to the bare SnO_2. Besides, the reduced interfacial recombination was correlated with the improved conductivity in SnO_2-cPCN ETL, preventing charge accumulation at the perovskite/ETLs interface [68]. A decrease in recombination at the perovskite/ETLs interface is conducive to promoting the V_{OC} and J_{SC}, resulting from the decreased trap density in ETLs. The result is highly consistent with PL and SCLC measurements.

Electrochemical impedance spectroscopy (EIS) was conducted to investigate the charge transport and recombination behavior. The semicircles in the low and

high-frequency regions are attributed to the recombination resistance (R_{rec}) and the transfer resistance (R_{tr}), respectively [69]. Figure 6a exhibits the Nyquist plots of the control and optimal devices in the dark with a bias of 0.5 V and a frequency from 0.1–10^5 Hz. It is revealed that the devices with the SnO_2-cPCN ETL have larger R_{rec} than the control device owing to the reduced surface/interface trap states and other recombination centers [70]. This behavior agrees with the increased carrier lifetime in TRPL and enhanced V_{OC} and J_{SC} of PSCs based on SnO_2-cPCN ETL. Since the SnO_2-cPCN-based devices presented outstanding performance with a small active area (0.1 cm^2), the large-area (active area, 1 cm^2) devices were further fabricated to assess the authenticity of cPCN in ETL of PSCs. The *J–V* curves measured from both directions are illustrated in Fig. 6b, and the inset shows the image of our large area device. The device generates a V_{OC} of 1.13 V, a J_{SC} of 24 mA cm^{-2}, an *FF* of 75%, and a *PCE* of 20.3% in the reverse scan. Similarly, the hysteresis of the devices is visibly reduced when cPCN was added to SnO_2 in large-area devices. Our previous characterizations have demonstrated the increased electron mobility with SnO_2-cPCN and the decreased trap density of the perovskite film deposited on SnO_2-cPCN, forming the primary reasons for reduced hysteresis.

3.3.4 *Stability Test*

Stability tests are a pivotal characterization of the PSCs. The long-term stability of unencapsulated PSCs fabricated with or without cPCN hybridization was investigated with the devices stored under dark in a glove box filled with nitrogen. As indicated in Fig. 6c, the device based on SnO_2-cPCN ETL maintains 95% of the original efficiency

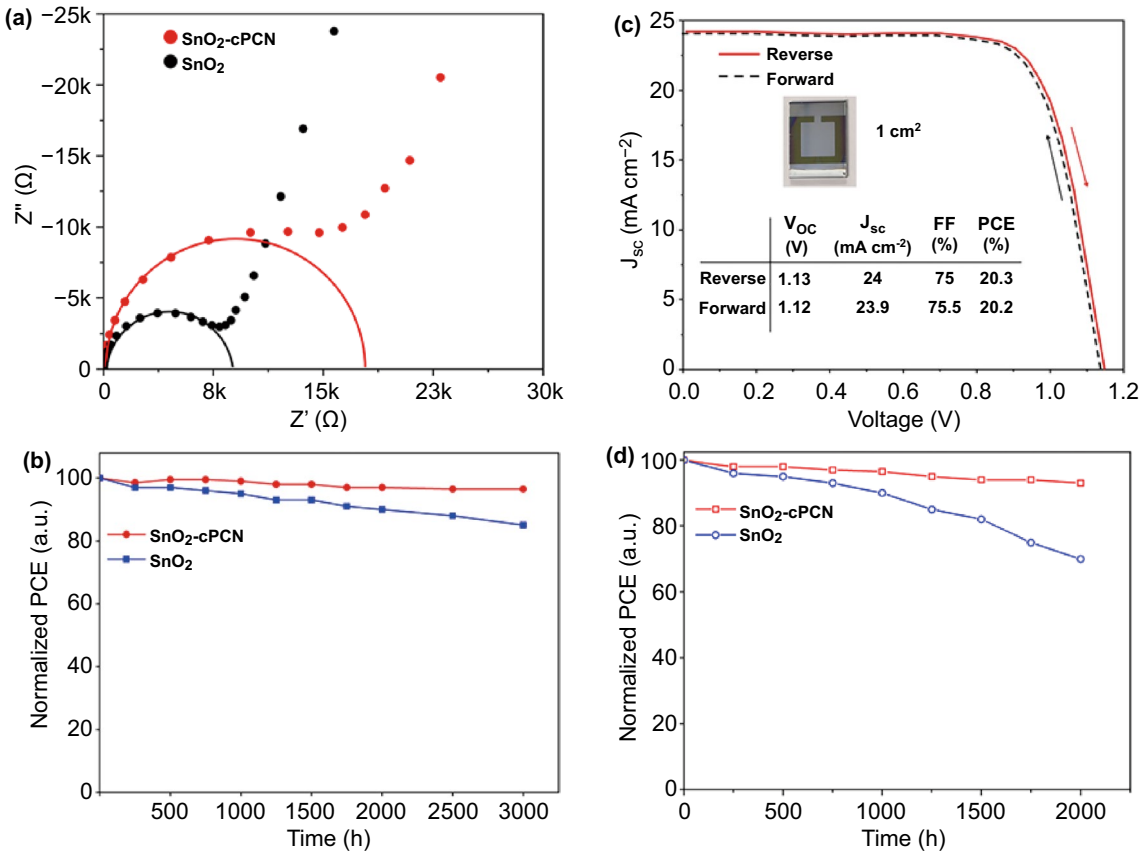

Fig. 6 **a** EIS of planar-type PSCs with SnO_2 and SnO_2-cPCN ETL, the insert picture is the fitting model. **b** *J–V* characteristics of the SnO_2-cPCN and SnO_2 based devices with a 1 cm^2 area (active area) in forward and reverse scan; the inset is a picture of real 1 cm^2 area devices. **c** Long-term stability measurements of devices without any encapsulation under N_2 glovebox, and **d** Humidity and oxygen stability under an ambient condition (relative humidity: 30% ± 5%)

https://doi.org/10.1007/s40820-021-00636-0

after 2880 h (~4 months). However, the device based on SnO_2 only keeps 85% of its initial efficiency under the same storage condition. Regarding the stability of PSCs under humidity and oxygen, the SnO_2-cPCN-based device also presents higher stability than SnO_2-based devices, maintaining 88% of the initial PCE after 2000 h of storage in the ambient environment (with controlled RH of 30% ± 5%) without any encapsulation (Figs. 6d and S13). For the same test duration, SnO_2-based devices remains only 64% relative to their initial efficiency. Apparently, the stability against oxygen, humidity, and long-term stability has been significantly improved with the increased quality of the perovskite film deposited on SnO_2-cPCN. The enhancement of stability can be attributed to the suppressed charge accumulation on the photoexcited perovskite and superoxide-mediated degradation pathway under the increased electron transfer with the SnO_2-cPCN ETL [71].

4 Conclusion

To sum up, a novel and effective SnO_2-cPCN composite yielding superior electron mobility of 3.3×10^{-3} $cm^2\ V^{-1}\ s^{-1}$ was produced. It is more than 3 times higher than that of neat SnO_2. Notably, the champion PCEs of the planar PSCs based on SnO_2-cPCN reached 23.17% on a small area device (0.1 cm^2), and the PCE of 20.3% was obtained on a 1 cm^2 device. The improved performance of the PSCs based on SnO_2-cPCN can be attributed to the following advantages. First, the surface wettability of SnO_2-cPCN slightly decreased after the cPCN addition, suppressing heterogeneous nucleation and enlarging perovskite grain size. Consequently, high-quality perovskite films with reduced grain boundaries and mitigated non-radiative recombination were generated. Second, the high electron mobility and improved band alignment of SnO_2-cPCN ETL reduced the charge accumulation at the perovskite/ETL interface, leading to negligible current density–voltage hysteresis. This work provides a promising direction for developing high-quality ETLs and verifies the enormous potential of large-scale deployment of perovskite photovoltaics.

Acknowledgements P. G. acknowledges the financial support from the National Natural Science Foundation of China (Grant No. 21975260).

Supplementary Information The online version contains supplementary material available at https://doi.org/10.1007/s40820-021-00636-0.

References

1. P. Gao, M. Grätzel, M. Nazeeruddin, Organohalide lead perovskites for photovoltaic applications. Energy Environ. Sci. **7**(8), 2448–2463 (2014). https://doi.org/10.1039/c4ee00942h
2. W.A. Dunlap-Shohl, Y. Zhou, N.P. Padture, D.B. Mitzi, Synthetic approaches for halide perovskite thin films. Chem. Rev. **119**(5), 3193–3295 (2019). https://doi.org/10.1021/acs.chemrev.8b00318
3. Z. Zhang, Z. Li, L. Meng, S.Y. Lien, P. Gao, Perovskite-based tandem solar cells: get the most out of the sun. Adv. Func. Mater. **30**(38), 2001904 (2020). https://doi.org/10.1002/adfm.202001904
4. A. Kojima, K. Teshima, Y. Shirai, T. Miyasaka, Organometal halide perovskites as visible-light sensitizers for photovoltaic cells. J. Am. Chem. Soc. **131**(17), 6050–6051 (2009). https://doi.org/10.1021/ja809598r
5. <best-research-cell-efficiencies.20200104.Pdf>
6. J.J. Yoo, S. Wieghold, M.C. Sponseller, M.R. Chua, S.N. Bertram et al., An interface stabilized perovskite solar cell with high stabilized efficiency and low voltage loss. Energy Environ. Sci. **12**(7), 2192–2199 (2019). https://doi.org/10.1039/c9ee00751b
7. M. Kim, G.-H. Kim, T.K. Lee, I.W. Choi, H.W. Choi et al., Methylammonium chloride induces intermediate phase stabilization for efficient perovskite solar cells. Joule **3**(9), 2179–2192 (2019). https://doi.org/10.1016/j.joule.2019.06.014
8. P. Wang, X. Zhang, Y. Zhou, Q. Jiang, Q. Ye et al., Solvent-controlled growth of inorganic perovskite films in dry environment for efficient and stable solar cells. Nat. Commun. **9**(1), 2225 (2018). https://doi.org/10.1038/s41467-018-04636-4
9. Y. Li, J. Shi, J. Zheng, J. Bing, J. Yuan et al., Acetic acid assisted crystallization strategy for high efficiency and long-term stable perovskite solar cell. Adv. Sci. **7**(5), 1903368 (2020). https://doi.org/10.1002/advs.201903368

10. H. Min, M. Kim, S. Lee, H. Kim, G. Kim, K. Choi et al., Efficient, stable solar cells by using inherent bandgap of a-phase formamidinium lead iodide. Science **366**(6466), 749–753 (2019). https://doi.org/10.1126/science.aay7044
11. J. Burschka, N. Pellet, S.J. Moon, R. Humphry-Baker, P. Gao et al., Sequential deposition as a route to high-performance perovskite-sensitized solar cells. Nature **499**(7458), 316–319 (2013). https://doi.org/10.1038/nature12340
12. T. Salim, S. Sun, Y. Abe, A. Krishna, A.C. Grimsdale et al., Perovskite-based solar cells: Impact of morphology and device architecture on device performance. J. Mater. Chem. A **3**(17), 8943–8969 (2015). https://doi.org/10.1039/c4ta05226a
13. T. Leijtens, G.E. Eperon, S. Pathak, A. Abate, M.M. Lee et al., Overcoming ultraviolet light instability of sensitized TiO_2 with meso-superstructured organometal tri-halide perovskite solar cells. Nat. Commun. **4**, 2885 (2013). https://doi.org/10.1038/ncomms3885
14. Q. Jiang, X. Zhang, J. You, SnO_2: A wonderful electron transport layer for perovskite solar cells. Small e1801154 (2018). https://doi.org/https://doi.org/10.1002/smll.201801154
15. W. Hui, Y. Yang, Q. Xu, H. Gu, S. Feng et al., Red-carbon-quantum-dot-doped SnO_2 composite with enhanced electron mobility for efficient and stable perovskite solar cells. Adv. Mater. **32**(4), e1906374 (2020). https://doi.org/10.1002/adma.201906374
16. M.M. Tavakoli, F. Giordano, S.M. Zakeeruddin, M. Gratzel, Mesoscopic oxide double layer as electron specific contact for highly efficient and uv stable perovskite photovoltaics. Nano Lett. **18**(4), 2428–2434 (2018). https://doi.org/10.1021/acs.nanolett.7b05469
17. Q. Jiang, Y. Zhao, X. Zhang, X. Yang, Y. Chen et al., Surface passivation of perovskite film for efficient solar cells. Nat. Photonics **13**(7), 460–466 (2019). https://doi.org/10.1038/s41566-019-0398-2
18. Y. Chen, S. Tan, N. Li, B. Huang, X. Niu et al., Self-elimination of intrinsic defects improves the low-temperature performance of perovskite photovoltaics. Joule **4**(9), 1961–1976 (2020). https://doi.org/10.1016/j.joule.2020.07.006
19. D. Yang, R. Yang, K. Wang, C. Wu, X. Zhu et al., High efficiency planar-type perovskite solar cells with negligible hysteresis using edta-complexed SnO_2. Nat. Commun. **9**(1), 3239 (2018). https://doi.org/10.1038/s41467-018-05760-x
20. W. Tress, N. Marinova, T. Moehl, S.M. Zakeeruddin, M.K. Nazeeruddin et al., Understanding the rate-dependent J–V hysteresis, slow time component, and aging in ch3nh3pbi3 perovskite solar cells: the role of a compensated electric field. Energy Environ. Sci. **8**(3), 995–1004 (2015). https://doi.org/10.1039/c4ee03664f
21. S.S. Shin, S.J. Lee, S.I. Seok, Metal oxide charge transport layers for efficient and stable perovskite solar cells. Adv. Funct. Mater. **29**(47), 1900455 (2019). https://doi.org/10.1002/adfm.201900455
22. Q. Xiong, L. Yang, Q. Zhou, T. Wu, C.L. Mai et al., $NdCl_3$ dose as a universal approach for high-efficiency perovskite solar cells based on low-temperature-processed SnO_x. ACS Appl. Mater. Interfaces **12**(41), 46306–46316 (2020). https://doi.org/10.1021/acsami.0c13296
23. X. Ren, D. Yang, Z. Yang, J. Feng, X. Zhu et al., Solution-processed Nb: SnO_2 electron transport layer for efficient planar perovskite solar cells. ACS Appl. Mater. Interfaces **9**(3), 2421–2429 (2017). https://doi.org/10.1021/acsami.6b13362
24. J. Wei, F. Guo, X. Wang, K. Xu, M. Lei et al., SnO_2 -in-polymer matrix for high-efficiency perovskite solar cells with improved reproducibility and stability. Adv. Mater. **30**(52), e1805153 (2018). https://doi.org/10.1002/adma.201805153
25. C. Bi, Q. Wang, Y. Shao, Y. Yuan, Z. Xiao et al., Non-wetting surface-driven high-aspect-ratio crystalline grain growth for efficient hybrid perovskite solar cells. Nat. Commun. **6**, 7747 (2015). https://doi.org/10.1038/ncomms8747
26. P. Murgatroyd, Theory of space-charge-limited current enhanced by frenkel effect. J. Phys. D **3**(2), 151 (1970). https://doi.org/10.1088/0022-3727/3/2/308
27. J. Xie, K. Huang, X. Yu, Z. Yang, K. Xiao et al., Enhanced electronic properties of SnO_2 via electron transfer from graphene quantum dots for efficient perovskite solar cells. ACS Nano **11**(9), 9176–9182 (2017). https://doi.org/10.1021/acsnano.7b04070
28. M. Hadadian, J.-H. Smått, J.-P. Correa-Baena, The role of carbon-based materials in enhancing the stability of perovskite solar cells. Energy Environ. Sci. **13**(5), 1377–1407 (2020). https://doi.org/10.1039/c9ee04030g
29. L.-L. Jiang, Z.-K. Wang, M. Li, C.-C. Zhang, Q.-Q. Ye et al., Passivated perovskite crystallization via g-c3n4 for high-performance solar cells. Adv. Funct. Mater. **28**(7), 1705875 (2018). https://doi.org/10.1002/adfm.201705875
30. Z. Li, S. Wu, J. Zhang, Y. Yuan, Z. Wang et al., Improving photovoltaic performance using perovskite/surface-modified graphitic carbon nitride heterojunction. Solar RRL **4**(3), 1900413 (2019). https://doi.org/10.1002/solr.201900413
31. J. Chen, H. Dong, L. Zhang, J. Li, F. Jia et al., Graphitic carbon nitride doped SnO_2 enabling efficient perovskite solar cells with pces exceeding 22%. J. Mater. Chem. A **8**(5), 2644–2653 (2020). https://doi.org/10.1039/c9ta11344d
32. F.K. Kessler, Y. Zheng, D. Schwarz, C. Merschjann, W. Schnick et al., Functional carbon nitride materials-design strategies for electrochemical devices. Nat. Rev. Mater. **2**(6), 17030 (2017). https://doi.org/10.1038/natrevmats.2017.30
33. L. Lin, H. Ou, Y. Zhang, X. Wang, Tri-s-triazine-based crystalline graphitic carbon nitrides for highly efficient hydrogen evolution photocatalysis. ACS Catal. **6**(6), 3921–3931 (2016). https://doi.org/10.1021/acscatal.6b00922
34. H. Gao, S. Yan, J. Wang, Y.A. Huang, P. Wang et al., Towards efficient solar hydrogen production by intercalated carbon nitride photocatalyst. Phys. Chem. Chem. Phys. **15**(41), 18077–18084 (2013). https://doi.org/10.1039/c3cp53774a
35. J. Zhang, M. Zhang, G. Zhang, X. Wang, Synthesis of carbon nitride semiconductors in sulfur flux for water photoredox catalysis. ACS Catal. **2**(6), 940–948 (2012). https://doi.org/10.1021/cs300167b

 https://doi.org/10.1007/s40820-021-00636-0

36. B. Tu, Y. Shao, W. Chen, Y. Wu, X. Li et al., Novel molecular doping mechanism for n-doping of SnO_2 via triphenylphosphine oxide and its effect on perovskite solar cells. Adv. Mater. **31**(15), e1805944 (2019). https://doi.org/10.1002/adma.201805944
37. M.F. Ayguler, A.G. Hufnagel, P. Rieder, M. Wussler, W. Jaegermann et al., Influence of fermi level alignment with tin oxide on the hysteresis of perovskite solar cells. ACS Appl. Mater. Interfaces **10**(14), 11414–11419 (2018). https://doi.org/10.1021/acsami.8b00990
38. J. Pei, Y. Wu, X. Guo, Y. Ying, Y. Wen et al., EmimBF4-assisted SnO_2-based planar perovskite films for label-free photoelectrochemical sensing. ACS Omega **2**(8), 4341–4346 (2017). https://doi.org/10.1021/acsomega.7b00496
39. S. Wang, Y. Zhu, B. Liu, C. Wang, R. Ma, Introduction of carbon nanodots into SnO_2 electron transport layer for efficient and uv stable planar perovskite solar cells. J. Mater. Chem. A **7**(10), 5353–5362 (2019). https://doi.org/10.1039/c8ta11651b
40. Q. Dong, Y. Fang, Y. Shao, P. Mulligan, J. Qiu et al., Electron-hole diffusion lengths >175 μm in solution-grown $CH_3NH_3PbI_3$ single crystals. Science **347**(6225), 967–970 (2015). https://doi.org/10.1126/science.aaa5760
41. D. Yang, X. Zhou, R. Yang, Z. Yang, W. Yu et al., Surface optimization to eliminate hysteresis for record efficiency planar perovskite solar cells. Energy Environ. Sci. **9**(10), 3071–3078 (2016). https://doi.org/10.1039/c6ee02139e
42. <physics of semiconductor devices.Pdf>.
43. P. Liu, W. Wang, S. Liu, H. Yang, Z. Shao, Fundamental understanding of photocurrent hysteresis in perovskite solar cells. Adv. Energy Mater. **9**(13), 1803017 (2019). https://doi.org/10.1002/aenm.201803017
44. Q. Jiang, L. Zhang, H. Wang, X. Yang, J. Meng et al., Enhanced electron extraction using $SnO_2$for high-efficiency planar-structure $HC(NH_2)_2PbI_3$-based perovskite solar cells. Nat. Energy **2**(1), 16177 (2016). https://doi.org/10.1038/nenergy.2016.177
45. S. Sonmezoglu, S. Akin, Suppression of the interface-dependent nonradiative recombination by using 2-methylbenzimidazole as interlayer for highly efficient and stable perovskite solar cells. Nano Energy **76**, 105127 (2020). https://doi.org/10.1016/j.nanoen.2020.105127
46. Y.H. Deng, Z.Q. Yang, R.M. Ma, Growth of centimeter-scale perovskite single-crystalline thin film via surface engineering. Nano Converg. **7**(1), 25 (2020). https://doi.org/10.1186/s40580-020-00236-5
47. N.J. Jeon, J.H. Noh, Y.C. Kim, W.S. Yang, S. Ryu et al., Solvent engineering for high-performance inorganic-organic hybrid perovskite solar cells. Nat. Mater. **13**(9), 897–903 (2014). https://doi.org/10.1038/nmat4014
48. G.E. Eperon, V.M. Burlakov, P. Docampo, A. Goriely, H.J. Snaith, Morphological control for high performance, solution-processed planar heterojunction perovskite solar cells. Adv. Funct. Mater. **24**(1), 151–157 (2014). https://doi.org/10.1002/adfm.201302090
49. W. Xu, Z. Lan, B.L. Peng, R.F. Wen, X.H. Ma, Effect of surface free energies on the heterogeneous nucleation of water droplet: A molecular dynamics simulation approach. J. Chem. Phys. **142**(5), 054701 (2015). https://doi.org/10.1063/1.4906877
50. X. Xiao, W. Li, Y. Fang, Y. Liu, Y. Shao et al., Benign ferroelastic twin boundaries in halide perovskites for charge carrier transport and recombination. Nat. Commun. **11**(1), 2215 (2020). https://doi.org/10.1038/s41467-020-16075-1
51. E.H. Jung, B. Chen, K. Bertens, M. Vafaie, S. Teale et al., Bifunctional surface engineering on SnO_2 reduces energy loss in perovskite solar cells. ACS Energy Lett. **5**(9), 2796–2801 (2020). https://doi.org/10.1021/acsenergylett.0c01566
52. S. You, H. Zeng, Z. Ku, X. Wang, Z. Wang et al., Multifunctional polymer-regulated SnO_2 nanocrystals enhance interface contact for efficient and stable planar perovskite solar cells. Adv. Mater. **32**(43), e2003990 (2020). https://doi.org/10.1002/adma.202003990
53. X. Chen, W. Xu, N. Ding, Y. Ji, G. Pan et al., Dual interfacial modification engineering with 2D MXene quantum dots and copper sulphide nanocrystals enabled high-performance perovskite solar cells. Adv. Funct. Mater. **30**(30), 2003295 (2020). https://doi.org/10.1002/adfm.202003295
54. B. Chen, M. Yang, X. Zheng, C. Wu, W. Li et al., Impact of capacitive effect and ion migration on the hysteretic behavior of perovskite solar cells. J. Phys. Chem. Lett. **6**(23), 4693–4700 (2015). https://doi.org/10.1021/acs.jpclett.5b02229
55. J.H. Heo, H.J. Han, D. Kim, T.K. Ahn, S.H. Im, Hysteresis-less inverted $CH_3NH_3PbI_3$ planar perovskite hybrid solar cells with 18.1% power conversion efficiency. Energy Environ. Sci. **8**(5), 1602–1608 (2015). https://doi.org/https://doi.org/10.1039/c5ee00120j
56. F. Zhang, D. Bi, N. Pellet, C. Xiao, Z. Li et al., Suppressing defects through the synergistic effect of a lewis base and a lewis acid for highly efficient and stable perovskite solar cells. Energy Environ. Sci. **11**(12), 3480–3490 (2018). https://doi.org/10.1039/c8ee02252f
57. W. Chen, Y. Wu, Y. Yue, J. Liu, W. Zhang et al., Efficient and stable large-area perovskite solar cells with inorganic charge extraction layers. Science **350**(6263), 944–948 (2015). https://doi.org/10.1126/science.aad1015
58. X. Yu, Q. Zhou, J. Xu, L. Liang, X. Wang et al., The impact of PbI_2: Ki alloys on the performance of sequentially deposited perovskite solar cells. Eur. J. Inorg. Chem. **9**, 821–830 (2021). https://doi.org/10.1002/ejic.202001109
59. T. Bu, J. Li, F. Zheng, W. Chen, X. Wen et al., Universal passivation strategy to slot-die printed SnO_2 for hysteresis-free efficient flexible perovskite solar module. Nat. Commun. **9**, 4609 (2018). https://doi.org/10.1038/s41467-018-07099-9
60. Y. Shao, Z. Xiao, C. Bi, Y. Yuan, J. Huang, Origin and elimination of photocurrent hysteresis by fullerene passivation in $CH_3NH_3PbI_3$ planar heterojunction solar cells. Nat. Commun. **5**, 5784 (2014). https://doi.org/10.1038/ncomms6784
61. T. Walter, R. Herberholz, C. Müller, H.W. Schock, Determination of defect distributions from admittance measurements and application to Cu(In, Ga)Se_2 based heterojunctions. J. Appl. Phys. **80**(8), 4411–4420 (1996). https://doi.org/10.1063/1.363401

62. S. Khelifi, K. Decock, J. Lauwaert, H. Vrielinck, D. Spoltore et al., Investigation of defects by admittance spectroscopy measurements in poly (3-hexylthiophene):(6, 6)-phenyl c61-butyric acid methyl ester organic solar cells degraded under air exposure. J. Appl. Phys. **110**(9), 094509 (2011). https://doi.org/10.1063/1.3658023
63. J.-W. Lee, D.-H. Kim, H.-S. Kim, S.-W. Seo, S.M. Cho et al., Formamidinium and cesium hybridization for photo- and moisture-stable perovskite solar cell. Adv. Energy Mater. **5**(20), 1501310 (2015). https://doi.org/10.1002/aenm.201501310
64. C. Ran, J. Xu, W. Gao, C. Huang, S. Dou, Defects in metal triiodide perovskite materials towards high-performance solar cells: origin, impact, characterization, and engineering. Chem. Soc. Rev. **47**(12), 4581–4610 (2018). https://doi.org/10.1039/c7cs00868f
65. M.-J. Choi, Y.-S. Lee, I.H. Cho, S.S. Kim, D.-H. Kim et al., Functional additives for high-performance inverted planar perovskite solar cells with exceeding 20% efficiency: Selective complexation of organic cations in precursors. Nano Energy **71**, 104639 (2020). https://doi.org/10.1016/j.nanoen.2020.104639
66. M. Maiberg, T. Hölscher, S. Zahedi-Azad, R. Scheer, Theoretical study of time-resolved luminescence in semiconductors. Iii. Trap states in the band gap. J. Appl. Phys. **118**(10), 105701 (2015). https://doi.org/https://doi.org/10.1063/1.4929877
67. Y. Li, L. Meng, Y.M. Yang, G. Xu, Z. Hong et al., High-efficiency robust perovskite solar cells on ultrathin flexible substrates. Nat. Commun. **7**, 10214 (2016). https://doi.org/10.1038/ncomms10214
68. D. Luo, R. Su, W. Zhang, Q. Gong, R. Zhu, Minimizing non-radiative recombination losses in perovskite solar cells. Nat. Rev. Mater. **5**(1), 44–60 (2019). https://doi.org/10.1038/s41578-019-0151-y
69. L. Liang, H. Luo, J. Hu, H. Li, P. Gao, Efficient perovskite solar cells by reducing interface-mediated recombination: a bulky amine approach. Adv. Energy Maters. **10**(14), 2000197 (2020). https://doi.org/10.1002/aenm.202000197
70. R. Wang, J. Xue, K.-L. Wang, Z.-K. Wang, Y. Luo et al., Constructive molecular configurations for surface-defect passivation of perovskite photovoltaics. Science **366**(6472), 1509–1513 (2019). https://doi.org/10.1126/science.aay9698
71. N. Aristidou, I. Sanchez-Molina, T. Chotchuangchutchaval, M. Brown, L. Martinez et al., The role of oxygen in the degradation of methylammonium lead trihalide perovskite photoactive layers. Angew. Chem. Int. Ed. **127**(28), 8326–8330 (2015). https://doi.org/10.1002/ange.201503153

 https://doi.org/10.1007/s40820-021-00636-0